Dynamics of an oil-coated bubble rising in a quiescent water medium

Bingqiang Ji,[1,*] Liu Hong,[1,*] Jin-Tae Kim,[1] Leonardo P. Chamorro,[1,2,3,4] and Jie Feng[1,5,†]
[1]*Mechanical Science and Engineering, University of Illinois at Urbana-Champaign, Urbana, Illinois 61801, USA*
[2]*Aerospace Engineering, University of Illinois at Urbana-Champaign, Urbana, Illinois 61801, USA*
[3]*Civil and Environmental Engineering, University of Illinois at Urbana-Champaign, Urbana, Illinois 61801, USA*
[4]*Geology, University of Illinois at Urbana-Champaign, Urbana, Illinois 61801, USA*
[5]*Materials Research Laboratory, University of Illinois at Urbana-Champaign, Urbana, Illinois 61801, USA*

(Received 3 October 2021; accepted 24 February 2022; published 14 March 2022)

We experimentally investigated the rising dynamics of oil-coated compound bubbles at various oil fractions in a quiescent water medium. Three-dimensional particle tracking velocimetry was used to characterize the trajectories of the bubbles, and particle image velocimetry was used for complementary flow characterization. Results show that the oil-coated bubbles undergo a zigzagging path with a steady oscillation pattern at comparatively low oil fractions. In contrast, damped oscillations occur at high oil fractions, which do not happen in clean gas bubbles. The oil coating changes the rising dynamics of the bubble mainly by adjusting the bubble surface boundary condition and effective density. A lightly coated bubble experiences a smaller shape deformation, similar drag coefficient, a larger frequency, and smaller amplitude in the path oscillation compared to a clean gas bubble. In addition, the increase of oil fraction results in reduced shape deformation and drag coefficient with a lower frequency and amplitude of the path oscillation. Estimation of the forces using a Frenet reference frame shows that the wake-induced lift and drag decreased with oil fraction, and became negligible for bubbles with damped oscillations. Overall, our work contributes to the fundamental understanding of the rising dynamics of oil-coated bubbles with various oil fractions and viscosities.

DOI: 10.1103/PhysRevFluids.7.033603

I. INTRODUCTION

Compounded bubbles with a liquid phase in another continuous bulk phase [1,2] are present in a wide range of natural and industrial processes, including gas released from natural seeps in the deep sea [3], froth flotation with oily bubbles [4,5], direct contact condensation [6–8], and three-dimensional (3D) printing by compound bubble writing [9]. Completely engulfed bubbles form when the coating and the bulk liquid are in a complete wetting state [10]. In nature or wasted water, compound bubbles with an organic coating such as an oil layer can scavenge dissolved toxins, bacteria, viruses, and particulate pollutants during rising [11–13]. The dynamics of oil-coated bubbles determines the bubble surface interactions with the surrounding fluid and thus the collection and transport rate of the organic matter [14,15]. Therefore, understanding the rising of compound bubbles is crucial for quantifying fundamental multiphase flows to control ecological and industrial processes.

*These authors contributed equally to this work.
†Corresponding author: jiefeng@illinois.edu

In fact, the dynamics of rising gas bubbles in liquids has been widely studied for over half a century. It is well known that millimetric bubbles rising in quiescent water undergo zigzag or spiral motions, which is mainly attributed to the wake instability [16]. Such a path instability appears at a sufficiently large Reynolds number [17], $\mathrm{Re} = \rho_w u d/\mu_w$, where asymmetric vortices coexist. Here, ρ_w is the water density, μ_w is the water viscosity, u is the bubble velocity, and d is the bubble diameter. In the zigzag regime, a pair of counterrotating streamwise vortices preserving a symmetry plane changes sign twice during a period of the rising path. Additionally, a pair of intertwined counterrotating vortices results in a frozenlike structure in the reference frame rotating with the bubble [18]. In addition, the wake/path instability can also be influenced by the bubble shape deformation [16], shape oscillation [19], and the surfactant effect that may modify the bubble's free-slip boundary condition into no-slip [20,21].

Experiments and numerical simulations have explored the forces on rising gas bubbles in quiescent liquids [22,23]; they suggest that the wake-induced force consists of not only a lift component controlling the lateral bubble motion, but also an additional drag producing slower rising. As a crucial parameter in predicting bubble motion, the drag coefficient has been expressed in a semiempirical way using a wide range of experimental data considering liquid properties and the bubble surface boundary condition [17,24,25]. The lift has also been modeled theoretically to predict zigzag or spiral trajectories [26,27]. In general, the rising bubble dynamics is also highly coupled with the surrounding bulk flow, exhibiting rich behavior in sheared and turbulent flows [28–30].

Most of the studies on compound bubbles have focused in particular on translation dynamics at relatively small Re. Sadhal and Johnson [31], Johnson and Sadhal [32], and Sadhal and Oguz [33] derived expressions for the drag coefficient taking into account the effects of the bubble configuration and the viscosity ratio of the coating liquid and the bulk medium at $\mathrm{Re} \ll 1$. Kawano and Hashimoto [34] and Kawano *et al.* [35] proposed expressions for drag coefficient applicable to Re of 200, which agreed with experimental results. Experimental studies of the compound bubbles rising at relatively high Re have only reported phenomenological observations and have ignored the path instability [36]; the proposed drag coefficient expressions exhibit large errors at a high Re regime compared with experiments [37]. Recently, Wang *et al.* [38] found experimentally and numerically that millimetric oil-coated bubbles rise in a zigzagging path with a smaller oscillation amplitude, weaker shape deformation, and smaller rising velocity compared to an uncoated counterpart, which is similar to a surfactant-contaminated bubble, while Karp *et al.* [39] reported experimentally that the drag coefficient for oil-coated bubbles at Re of 60–700 exhibits intermediate values compared to corresponding single-fluid drops and bubbles. However, the influence of the oil coating, especially the oil fraction, on the bubble rising dynamics is still unclear. In particular, the characterization of the compound bubble's path instability remains an open question.

Here, we investigate experimentally the rising dynamics of oil-coated bubbles at $\mathrm{Re} \approx 10^3$, focusing on the effect of oil fraction and the resulting wake-induced forces on the bubble trajectory. The experimental setup is described in Sec. II. In Sec. III, we analyze the quasisteady bubble shape, zigzagging bubble trajectory, as well as terminal velocity and drag coefficient. The path oscillation and wake instability are assessed with the forces acting on the bubble. Finally, a discussion and main conclusions are provided in Sec. IV.

II. EXPERIMENTS

A. Experimental setup

Experiments were performed in an acrylic tank filled with deionized water. The dimensions of the tank, 60 mm × 60 mm × 220 mm, were designed to avoid boundary effects on the dynamics of a rising bubble. Coaxial orifices were added at the bottom of the tank with a small stainless-steel needle inserted into a large one. The inner needle was located at the center and above the outer needle exit. Oil and gas were injected using two syringe pumps (PHD ULTRA, 11 Pico Plus Elite,

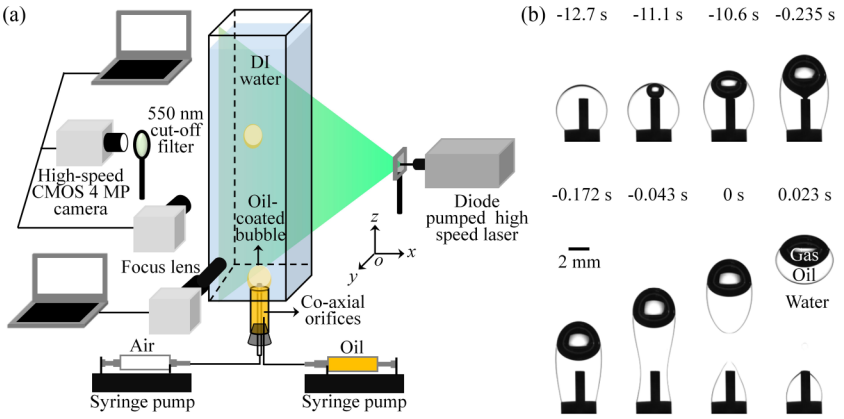

FIG. 1. (a) Schematic of the experimental setup illustrating the generation of oil-coated bubbles with coaxial orifices. (b) Time sequence showing the formation process of a 10 cSt silicone oil-coated bubble of $d = 4.38$ mm and $\phi_o = 0.54$.

Harvard Apparatus) through the outer and inner needles to generate oil-coated bubbles. A 1024 × 1024 pixels, high-speed camera (FASTCAM Mini AX200, Photron) mounted with a Navitar 12× zoom lens system was used to capture the bubble formation and detachment processes at a frequency 2000 Hz with an exposure time of 50 or 100 μs. A basic schematic of the experimental system is shown in Fig. 1(a). The properties of the deionized (DI) water and silicone oils are listed in Table I; the surface tensions of the liquids and their interfacial tensions were measured using the pendant-drop method.

Two 4 MP CMOS cameras were mounted perpendicularly to track the motion of the center of the bubbles. Illumination was provided by uniform LED light panels placed at one of the sides of the tank. The generalized Laplacian of Gaussian (gLoG) method was used to accurately position the bubbles center regardless of bubble deformation and size [40]. The trajectories were tracked using the nearest method by a single frame gap closing to obtain a path from the moment of release at the needle tip to the moment of the bubble rising to the water surface [41]. The 3D trajectories and temporal derivatives of the bubble motion were reconstructed using fourth-order B splines [42]. More details about the tracking method can be found in [43]. The oil-coated bubble shape evolution at the zigzag stage was visualized using two high-speed cameras mounted with a macrolens under the illumination of two LED panels.

Complementary in-plane flow velocity measurements were carried out with a particle image velocimetry (PIV) system from TSI. The flow was seeded with 14 μm silver-coated, hollow glass spheres with a density of 1300 kg m^{-3}. A high-speed, 50 mJ dual cavity YLF laser from Terra was used to illuminate a field of view (FOV) of 200 mm × 60 mm. A total of 400 image pairs were collected at a frequency of 200 Hz with a 4 MP (2560 pixels × 1600 pixels) high-speed, 12-bit CMOS Phantom Miro 340 camera. The image pairs were interrogated with a recursive cross-correlation method using the Insight 4G software from TSI. The final interrogation window resulted in 16 × 16 pixels with 50% overlap, resulting in a final vector grid spacing of $\Delta x = \Delta y = 600$ μm.

TABLE I. Basic properties of the fluids used in the experiments; a, air; o, oil; and w, water.

Fluid	ρ (kg m^{-3})	μ (mPa s)	γ_{wa} (mN m^{-1})	γ_{ow} (mN m^{-1})	γ_{oa} (mN m^{-1})
DI water	998	0.89	71.6 ± 1.0	N/A	N/A
10 cSt silicone oil	930	9.3	N/A	40.9 ± 0.5	19.1 ± 0.3
100 cSt silicone oil	960	96	N/A	43.7 ± 0.4	20.1 ± 0.2

B. Oil-coated bubble formation at coaxial orifices

The generation of an oil-coated bubble consisted of two distinct processes. First, a sessile oil droplet of volume V_o^i was produced above the outer needle; then, a gas bubble was generated in the oil droplet by injecting air through the inner needle at a small flow rate ($\leqslant 50$ μL/min) to ensure a quasistatic formation. The gas bubble grew with its top coated by an oil film, and then pinched off and detached from the inner needle. The gas bubble rose under buoyancy and stretched the oil below it into an oil column; after the oil column pinched off, an oil-coated bubble was formed [Fig. 1(b)]. Because of the complete wetting state of silicone oil at the water/gas interface, the formed bubble was completely encapsulated by the oil, and it rose with an oil tail at the bottom after the release. The volumes of the gas, V_g, and oil, V_o, of the oil-coated bubbles were calculated by imaging the initial rising bubble. Then, the equivalent diameter d and oil volume fraction ϕ_o of the oil-coated bubble were quantified as

$$d = \left(6\frac{V_g + V_o}{\pi}\right)^{1/3} \tag{1}$$

and

$$\phi_o = \frac{V_o}{V_g + V_o}. \tag{2}$$

d and ϕ_o can be controlled by adjusting the size of the coaxial orifices and V_o^i as shown by our previous study [44,45]. We used bubbles with $d = 4.22 \pm 0.22$ mm and $\phi_o = 0.04$–0.61 in the current experiments.

III. RESULTS

A. Quasisteady compound bubble shape

After being released from the coaxial orifices, the pinch-off of the oil column induced a bubble shape oscillation that damped quickly; then, the oil-coated bubble rose vertically with a steady shape in a rectilinear path before the onset of path instability. Figures 2(a) and 2(b) illustrate quasisteady shapes of the gas and oil-coated bubbles with different oil viscosities and oil fractions. The oil-coated bubble exhibited an oblate ellipsoidal shape with its minor (shorter) axis aligned with the motion direction. The majority of the oil was distributed at the bottom of the bubbles as an oil tail due to the larger oil density. A thin oil film persisted on the rest of the gas bubble surface considering the complete wetting state of the silicone oil [38]. The evolution of the oil layer thickness (h_o) along the surface of 10 cSt silicone oil-coated bubbles is shown in Fig. 2(c), where β is the angular position on the gas bubble surface. It shows that h_o is the largest at the bottom and decreases toward the sides, where the maximum oil layer thickness increases with ϕ_o. We define the aspect ratio of the oil-coated bubble χ as the size ratio of the major (longer) axis a to the minor axis (or principal axis for an oblate ellipsoid) b, i.e., $\chi = a/b$; its variation with the oil fraction ϕ_o is shown in Fig. 2(d), which shows that χ decreases significantly with a comparatively small amount of oil comparing a lightly coated bubble ($\phi_o \leqslant 0.08$) with the gas bubble, and it decreases slowly with ϕ_o for the oil-coated bubbles.

The deformation of the bubble is mainly caused by inertia and buoyancy while resisted by the surface tension and viscous force [46], which involves the Reynolds (Re), Weber (We $= \rho_w u^2 d/\gamma_e$), and Bond [or Eötvös, Bo $= (\rho_w - \rho_b)gd^2)/\gamma_e$] numbers [25,46]. Here, we use $\gamma_e = \gamma_{wa}$ for a gas bubble and $\gamma_e = \gamma_{ow}$ for oil-coated bubbles; g is the gravitational acceleration, and ρ_b is the effective compound bubble density, defined as

$$\rho_b = \rho_g(1 - \phi_o) + \rho_o\phi_o. \tag{3}$$

The velocity boundary condition of the bubble also plays an important role in the bubble deformation since it can alter the inertia and viscous force by modifying the flow field and the pressure

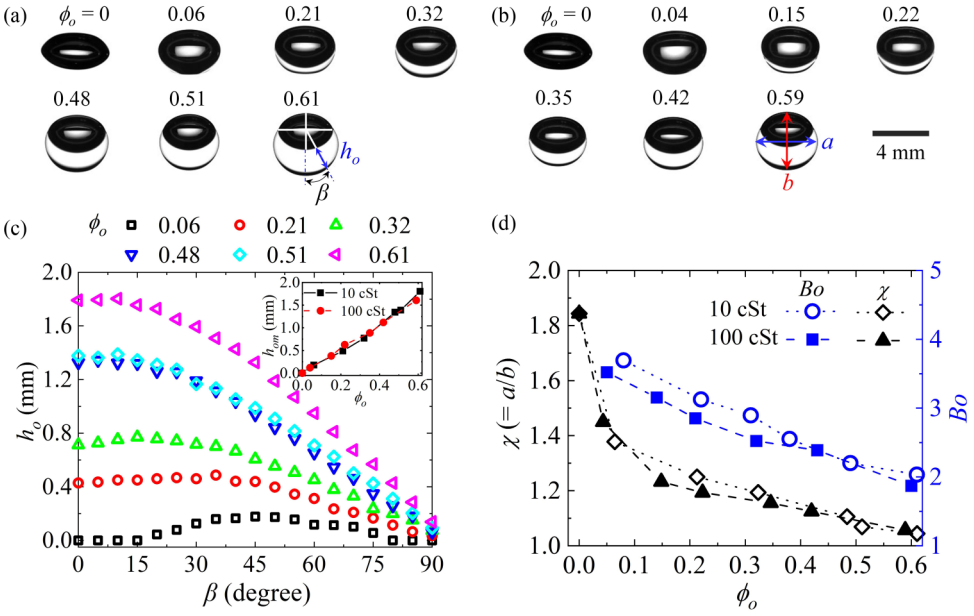

FIG. 2. Quasisteady compound bubble shapes before the onset of path instability. (a) 10 cSt silicone oil-coated bubble with oil fractions of 0, 0.06, 0.21, 0.32, 0.48, 0.51, and 0.61, and (b) 100 cSt silicone oil-coated bubble with oil fractions of 0, 0.04, 0.15, 0.22, 0.35, 0.42, and 0.59. Subpanel (b) shows the definition of the aspect ratio of the compound bubble, $\chi = a/b$, where a and b are the major (longer) and minor axes of the compound bubble. (c) Oil layer thickness h_o as a function of the angular position on the gas bubble surface β for the 10 cSt oil-coated bubbles shown in (a). The insets show the maximum oil layer thickness h_{om} as a function of the oil fraction ϕ_o for 10 and 100 cSt silicone oil-coated bubbles. The measurement error for the film thickness is less than 40 μm. The oil layer thickness below 80 μm is not included due to imaging resolution limitation. (d) Aspect ratio χ and Bond number Bo as a function of ϕ_o for the bubbles in (a) and (b).

distribution around the bubble. Here, Re $\approx$ 1000 for all the cases, thus Bo, We, and the bubble boundary condition determine the bubble deformation. By boundary here we mean the interface between the compound bubble (oil+gas) and surrounding water for oil-coated bubbles.

The smaller χ of lightly coated bubbles compared with clean gas bubbles is caused by the change of bubble velocity boundary condition (no-slip for clean bubbles and free-slip for oil-coated bubbles). Comparison of the lightly coated bubbles with the gas counterparts indicates that We and Bo increase due to the decrease of γ_e. This means a decreasing surface tension effect, which should enhance the bubble deformation if the boundary condition stays the same. However, Fig. 2(d) shows that the χ of lightly coated bubbles is much smaller than a gas bubble, indicating that oil coating also changed the bubbles' boundary condition during rising. According to the experimental images, the lightly coated bubble had an oil layer thinner than 200 μm, as shown in Figs. 2(a) and 2(b). The motion within such a thin viscous oil coating is largely inhibited compared to a clean gas bubble, as evidenced by Kawano and Hashimoto [47] with a Re up to 200, presumably rendering an approximately no-slip boundary condition. Comparatively, a clean gas bubble has a free-slip boundary. This yields a surface pressure distribution closer to that of the inviscid potential flow with higher pressure at the rear and lower pressure at the sides [48]. It results in a high deformation (χ) compared to a fully contaminated bubble with a no-slip boundary [24], as confirmed by observations on the surfactant effect on the shape of rising bubbles [20].

On the other hand, the decreasing χ with ϕ_o for the oil-coated bubbles is attributed to the increase of effective bubble density ρ_b. We also conducted PIV experiments to characterize the flow in the oil coating before the onset of path instability at Re of the oil-coated bubble up to 1000 to

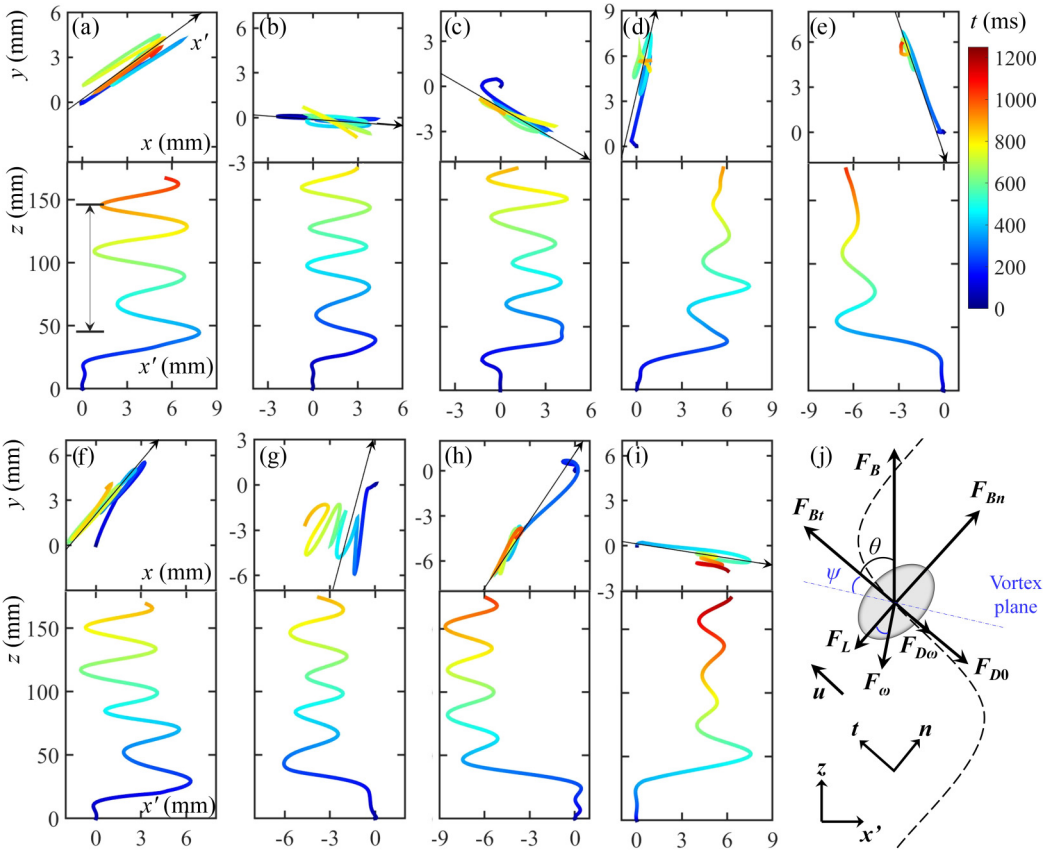

FIG. 3. Top x-y and side x'-z views of bubble trajectories colored by the residence time t after the release. (a) Gas bubble; 10 cSt silicone oil-coated bubbles with oil fractions of (b) 0.08, (c) 0.22, (d) 0.38, and (e) 0.61; 100 cSt silicone oil-coated bubbles with oil fractions of (f) 0.05, (g) 0.21, (h) 0.43, and (i) 0.60. Time $t = 0$ represents the moment of the release from the coaxial orifice. The black line in the top view represents the dominant x'-z plane of the bubble motion. (j) Diagram of the coordinate systems. The dashed line represents the bubble trajectory. A zigzagging bubble suffers from the driving buoyant force F_B, drag forces $F_{D\omega}$ and F_{D0}, and the lift force F_L. F_L (in the $\boldsymbol{n}$ direction normal to $\boldsymbol{t}$ direction) and $F_{D\omega}$ (in the motion direction $\boldsymbol{t}$) are the components of the wake-induced force F_ω in a Frenet reference frame (t, n, b). F_ω is at right angles to a plane (vortex plane) through the two vortex threads.

verify the motion in the oil coating and bubble boundary condition. The PIV results show that there are negligible recirculation flows in the oil coating. Therefore, it is considered as a nearly no-slip boundary condition for all the compound bubbles. We also note that We is nearly unaffected by ϕ_o, whereas Bo decreased significantly due to the ρ_b increase with ϕ_o [Fig. 2(d)]. This indicates a reduced buoyancy effect, resulting in decreased χ for the oil-coated bubbles. For the same oil fraction, χ of 10 and 100 cSt oil-coated bubbles are comparable [Fig. 2(d)] due to the similar boundary condition and Bo.

B. Bubble zigzagging

1. Bubble trajectory

Figures 3(a)–3(i) illustrate the top x-y and side x'-z plane views of the trajectory of the gas and oil-coated bubbles after the release. The top view shows that the bubbles mainly rose in a planar

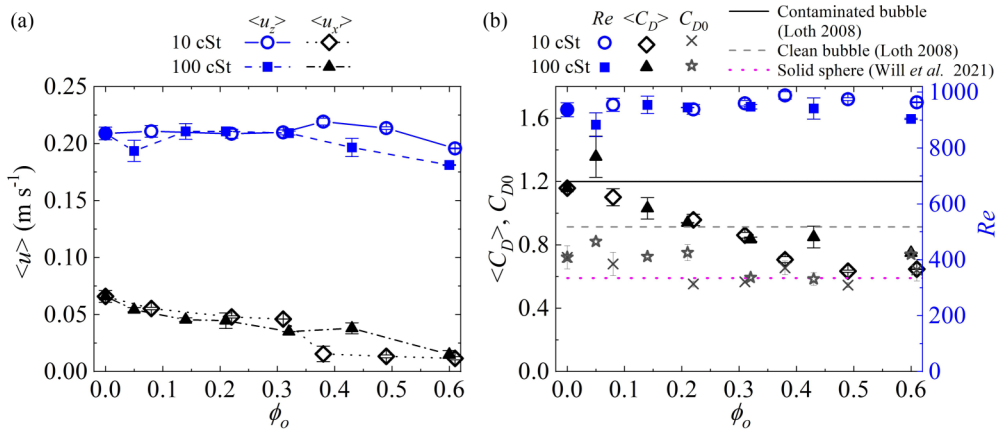

FIG. 4. (a) Terminal velocity $\langle u_z \rangle$ and time-average transverse speed $\langle u_{x'} \rangle$ as a function of the bubble's oil fraction ϕ_o. (b) Average drag coefficient $\langle C_D \rangle$ as a function of ϕ_o; the drag coefficient C_{D0} assumes an axisymmetric wake. The solid and dashed lines in (b) represent $\langle C_D \rangle$ of 4.2 mm diameter clean and surfactant-contaminated ellipsoidal gas bubbles rising in water at Re $\approx$ 1000 [24]; the dotted line represents $\langle C_D \rangle$ of a light solid sphere rising in water at Re $\approx$ 9000 [52].

motion determined as the dominant plane x'-z by principal component analysis [49]. The side view trajectory illustrated in this plane shows that the bubbles rose nearly straight for a short distance before undergoing zigzagging paths. Rectilinear and zigzag or spiral bubble rising behaviors can be determined by Bo and the Galilei number, $\mathrm{Ga} = \rho_w(1-\rho_b/\rho_w)^{1/2} g^{1/2} d^{3/2}/\mu_w$ [50]. Here, Bo $\approx$ 1.89–3.69 and Ga $\approx$ 671–888, which is representative of asymmetric trajectories for gas bubbles [51]. We found that the onset of path instability is delayed by the increase of oil fraction. Similar to the gas bubble, the path oscillation amplitude of the oil-coated bubbles during the zigzag stage was steady when ϕ_o was relatively small, which is denoted as a steady oscillation. Remarkably, the path oscillation amplitude continuously damped with time (denoted as a damped oscillation) when ϕ_o was equal to or larger than a critical value ϕ_{oc}, which is about 0.38 for 10 cSt oil-coated bubbles and 0.6 for 100 cSt oil-coated bubbles. The oil-coated bubbles with $\phi_o \geqslant \phi_{oc}$ tended to rise rectilinearly again after the damped path oscillation. It is worth pointing out that the bubbles may reach a spiral motion after rising with a zigzagging path for a distance of more than several hundred bubble diameters [16,22], which is far beyond the rising distance we study here.

2. *Terminal velocity and drag coefficient*

The rising velocity of the bubbles increased comparatively quickly after the release and reached the maximum at the end of the rectilinear stage; then, they oscillated around a mean terminal velocity periodically during the zigzag stage. The terminal velocity $\langle u_z \rangle$ and average transverse speed $\langle u_{x'} \rangle$ were calculated as the time-average vertical and transverse speeds between the second and the second-to-last peaks in the zigzag stages [as marked in Fig. 3(a)]. As shown in Fig. 4(a), $\langle u_{x'} \rangle$ is much smaller than $\langle u_z \rangle$, first decreasing slowly with ϕ_o when ϕ_o is small, and then reaching to near zero at ϕ_{oc} corresponding to the occurrence of the damped path oscillation. The $\langle u_z \rangle$ is independent of ϕ_o and stays about 0.21 m s^{-1} when ϕ_o is small, and it decreases when $\phi_o \geqslant 0.61$ for 10 cSt oil-coated bubbles and $\phi_o \geqslant 0.43$ for 100 cSt oil-coated bubbles.

We can further infer the drag coefficient by measuring the bubble's terminal velocity. The bubbles reach the terminal velocity when the time-averaged forces on the bubble in the vertical direction are balanced, i.e., the driving buoyant force

$$F_B = (\rho_w - \rho_b)\frac{\pi}{6} d^3 g \tag{4}$$

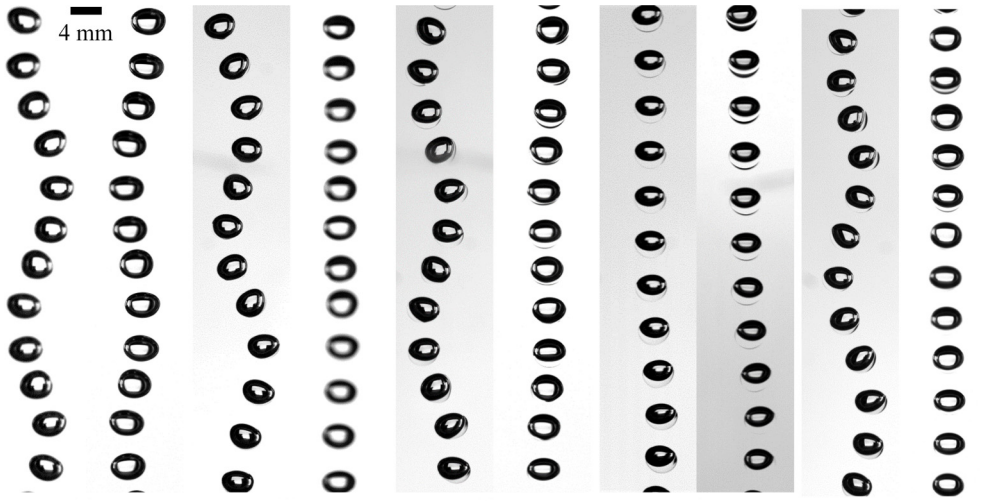

FIG. 5. Image sequence of the bubble's shape during the zigzag stage. (a) Gas bubble. 10 cSt silicone oil-coated bubbles with oil fractions of (b) 0.06, (c) 0.20, and (d) 0.39. (e) 100 cSt silicone oil-coated bubble with an oil fraction of 0.20. The left and right panels in the subfigures are obtained from perpendicular views. The images are superimposed every $\Delta t = 25$ ms.

is counteracted with the time-average drag force

$$\langle F_D \rangle = \langle C_D \rangle \frac{\pi}{8} d^2 \rho_w \langle u_z \rangle^2, \tag{5}$$

yielding the time-average drag coefficient $\langle C_D \rangle$ as

$$\langle C_D \rangle = \frac{4(1 - \rho_b/\rho_w) dg}{3\langle u_z \rangle^2}, \tag{6}$$

which is a crucial parameter of bubble rising dynamics. The estimation of $\langle C_D \rangle$ using Eq. (6) is shown in Fig. 4(b). C_{D0} in Fig. 4(b) represents the drag coefficient assuming an axisymmetric wake, which is calculated from Eq. (6) using the maximum bubble velocity u_m at the rectilinear rising stage [20]. It is well known that $\langle C_D \rangle$ of bubbles is primarily dependent on Re [24], while also affected by χ and We [25,53]. For the oil-coated bubbles in this study, Re $\approx$ 945 [Newton's drag regime, Fig. 4(b)] and We $\approx$ 3.9. We found that $\langle C_D \rangle$ of the oil-coated bubbles decreases from 1.35 to 0.63 with increasing ϕ_o, consistent with $\langle C_D \rangle$ shown by Will *et al.* [52] for an oblate ellipsoid with a density of $0.5\rho_w$ and a high Re, regarding a similar χ value in our experiments. Figure 5 illustrates that the variation of the bubble shape at zigzag stages is comparatively small; it can be evaluated using the quasisteady χ in Fig. 2. The bubbles align their minor axis with the motion direction; they rise in a broadside orientation, as noted by studies on oblate bubble rising [20,22,23]. Therefore, the decrease of $\langle C_D \rangle$ of the oil-coated bubble can be mainly attributed to the decrease of the frontal area, which reduces flow separation [54,55], while the no-slip velocity boundary condition remains the same. In addition, $\langle C_D \rangle$ of bubbles coated with different viscosity oils overlap with each other, which is consistent with that of the solid sphere rising [52]. This indicates a nearly immobile surface of the oil-coated bubble due to high μ_o.

For the gas bubble, $\langle C_D \rangle \approx 1.15$, slightly larger than that reported by Loth [24], which may be caused by slight contamination of the PIV tracer particles [56]. For the lightly coated bubble, though with a much smaller χ, $\langle C_D \rangle$ is similar or larger than the gas bubble. Loth [24] reported $\langle C_D \rangle \approx 1.2$ for contaminated bubbles of the same Re, because the drag force is enlarged by the flow separation when the bubble surface becomes contaminated and immobile [21,57].

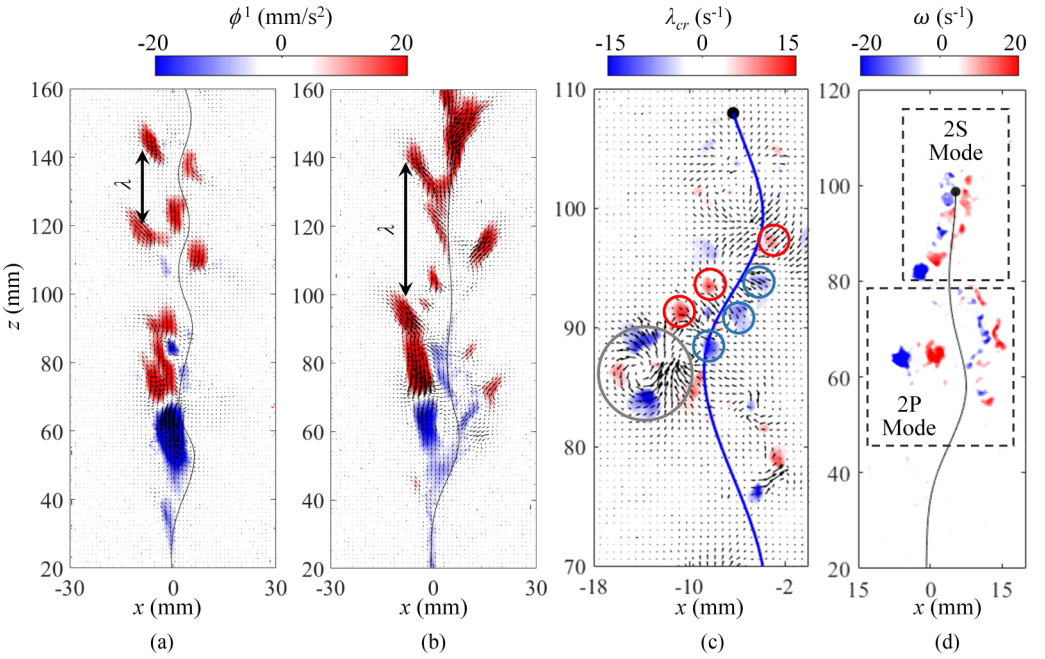

FIG. 6. Spatial organization of the first velocity component POD mode ϕ^1: (a) steady oscillation case (100 cSt silicone oil-coated bubble with $\phi_o = 0.14$); (b) damped oscillation case (100 cSt silicone oil-coated bubble with $\phi_o = 0.6$). (c) Snapshot of the swirling strength λ_{ci} in the wake region of a steady oscillating bubble when $t = 495$ ms (10 cSt silicone oil-coated bubble with $\phi_o = 0.22$). The solid line represents the bubble history trajectory, while the black solid sphere represents the compound bubble position. (d) Snapshot of the vorticity ω in the wake region of a damped oscillating bubble (100 cSt silicone oil-coated bubble with $\phi_o = 0.6$) when $t = 750$ ms, showing the two-pair (2P) to two-single (2S) transition of the wake mode.

3. Wake instability

We performed a complementary inspection of the trace left by the motion of the bubble to explore the connection of path and wake instability. Dominant coherent structures are obtained with snapshot proper orthogonal decomposition (POD) following Sirovich [58]. Velocity fluctuations $\boldsymbol{u}'(\boldsymbol{x}, t)$ are decomposed into a deterministic spatially correlated part $\phi^n(\boldsymbol{x})$ and time-dependent coefficients $a^n(t)$ as follows:

$$\boldsymbol{u}'(\boldsymbol{x}, t) = \sum_{n=1}^{N} a^n(t)\boldsymbol{\phi}^n(\boldsymbol{x}). \tag{7}$$

Here, $N \approx 200$ represents the number of snapshots. POD extracts modes that optimize the mean-square value of the velocity fluctuation by utilizing singular value decomposition (SVD) [59]. Then, the contribution of each mode to the turbulence kinetic energy is sorted based on the corresponding ratio of the eigenvalue to summation of the N eigenvalues, i.e., $E_n = \lambda_n / \sum_{m=1}^{N} \lambda_m$. Figures 6(a) and 6(b) show the dominant first POD mode $\phi^1(\boldsymbol{x})$, uncovering periodic vortex formation along the bubble trajectories. They indicate a vortex shedding frequency $f_v = 2u_t/\lambda$ using the wavelength λ given in Fig. 6; this indicates that the bubble oscillation frequency is mainly modulated by vortex frequency $f_v \approx 2f$, showing that the path oscillation corresponds to the vortex shedding.

A close inspection of the comparatively high-shear region in the vicinity of the bubbles' path reveals the formation of Kelvin-Helmholtz (KH) -type instability, as highlighted in the blue and red colored circles in Fig. 6(c). These motions merge to form larger coherent vortices illustrated in

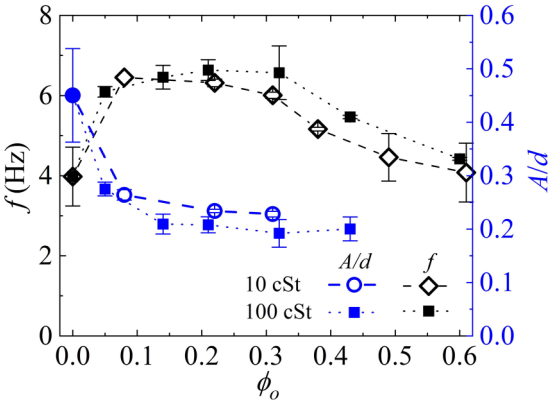

FIG. 7. Path oscillation frequency f and amplitude A scaled with the compound bubble diameter d as a function of the bubble's oil fraction, ϕ_o. For damped path oscillation cases ($\phi_o \geqslant \phi_{oc}$), A decreased over time and thus is not shown here.

the POD characterization [60]. Figure 6(c) shows instantaneous vortical structures using the signed swirling strength λ_{ci}, which is the magnitude of the imaginary part of complex eigenvalues of the velocity gradient tensor [61].

4. Path oscillation frequency and amplitude

The path oscillation frequency f and amplitude A of the bubbles during the zigzag stage are shown in Fig. 7. They are calculated by measuring the average crest-to-crest time duration and half of the lateral distance between the second and the second-to-last peaks, respectively. The oscillation frequency of a lightly coated bubble increased significantly, reaching about 1.6 times that of the gas bubble. This is consistent with observations from Tagawa *et al.* [20], where f of a fully contaminated bubble was about 1.8 times that of the gas bubble. Similar to bubbles contaminated by surfactants, the immobility of the surface of the lightly coated bubble largely enhanced the flow separation and promoted vortex shedding, thus resulting in a larger f compared to a clean gas bubble. In addition, f decreased with ϕ_o for oil-coated bubbles, since smaller χ results in weaker vorticity generation [16]. The vorticity generated on an oblate bubble may be estimated as $\omega \sim u\kappa$ at a sufficiently large Re, where κ is the surface curvature [62]. For an ellipsoidal bubble, the vorticity is mainly generated around the largest curvature $\kappa \sim \chi^{5/3}/d$ [26]; thus $\omega \sim u\chi^{5/3}/d$. Then, the vorticity generated on the bubble surface is shed downstream by the combined action of the viscous diffusion and the asymmetric transport via the vortex shedding [16]. Suppose we neglect the viscous diffusion considering the large Re and assume that the critical vorticity given at the onset of vortex shedding does not change under similar Re. In that case, the vortex shedding should be more frequent, and thus f (which is consistent with the vortex shedding frequency as discussed in Sec. III C) becomes larger with increasing χ. Based on this argument, we can estimate that the f of the bubble with $\phi_o \approx 0.05$ is 1.62 times that of the bubble with $\phi_o \approx 0.6$ due to a large χ, agreeing well with our experimental results.

The path oscillation amplitude, A, largely decreased even for lightly coated bubbles compared to a gas bubble; it is indeed nearly independent of ϕ_o for oil-coated bubbles. The magnitude of A is modulated by the wake-induced lift F_L (the force driving the bubbles' lateral motion) and the path oscillation frequency f (determining the acting time of F_L at a single oscillation period). Comparing the lightly coated bubble with the clean gas bubble shows that F_L is almost unchanged, as indicated by the acting force analysis in Sec. III C 2. In contrast, f is larger and thus results in a smaller A. Tagawa *et al.* [20] also reported a smaller A but similar F_L for a fully contaminated bubble than a clean gas bubble. For the oil-coated bubbles with increasing ϕ_o, F_L decreases as shown in

Sec. III C 2, and f also decreases. These two effects may compensate with each other and then result in a nearly constant A for oil-coated bubbles with a steady oscillation. A numerical study by Mougin and Magnaudet [16] also reported a constant A and a decreasing f with χ in the zigzag regime of freely rising ellipsoidal bubbles of a constant free-slip surface, similar to our results for oil-coated bubbles of a nearly constant no-slip surface with increasing ϕ_o (or χ). For damped path oscillation cases ($\phi_o \geqslant \phi_{oc}$), A decreased over time and thus it is not shown in Fig. 7, and more discussions can be found in Sec. III D. Considering the importance of wake dynamics on the variations of C_D, f, and A, we will further discuss the acting forces, especially the wake-induced force on an oil-coated bubble, in Sec. III C.

C. Force analysis on the rising dynamics

In this section, we analyze the forces, especially the wake-induced forces, acting on the compound bubble based on the bubble motion equation to understand further the effect of oil coatings on the wake/path instability of the rising bubble. First, we provide the theoretical model, then we discuss the acting forces on bubbles with different coatings inferred from the measured bubble trajectory and velocity.

1. Basic theoretical model

The motion of a fixed-shape body moving in a quiescent fluid can be described using the classical Kelvin-Kirchhoff equation based on potential flow theory [63]. It has been successfully applied to measure the wake-induced forces acting on rising gas bubbles [20,22] and rigid objects [52,64], and to simulate bubble motion undergoing a path instability [16,23]. As shown in Fig. 5, the compound bubble shape remains approximately unchanged during the zigzag stage under relatively low oscillations, which is similar to that of gas bubbles reported by Shew *et al.* [22]. Thus, taking the whole compound bubble, including the gas and oil, into consideration, we analyze the rising of a fixed-shape ellipsoid, assuming the compound bubble shape centroid as the mass center. Based on the Kelvin-Kirchhoff equation, the translation motion equation of an oil-coated bubble can be expressed as

$$(m\mathsf{I} + \mathsf{A}) \cdot \frac{d\boldsymbol{u}}{dt} + \boldsymbol{\Psi} \times (m\mathsf{I} + \mathsf{A}) \cdot \boldsymbol{u} = \boldsymbol{F}_H + \boldsymbol{F}_B, \tag{8}$$

where I is the identity tensor, A is the added mass tensor, $m = \rho_b \pi d^3/6$ is the bubble mass, $\boldsymbol{\Psi}$ is the bubble's rotational angular velocity about the instantaneous position of its axes, and $\boldsymbol{F}_H$ is the hydrodynamic force. The dynamic quantities in Eq. (8) are measured experimentally in the Galilean reference frame (x', y', z) and projected onto a Frenet reference frame (t, n, b), which moves and rotates along with the bubble with the tangent to the path curve $\boldsymbol{t}$, the normal to the path curve $\boldsymbol{n}$, and the binormal $\boldsymbol{b}$ as unit vectors, as illustrated in Fig. 3(j).

As shown in Fig. 3, the bubble motion occurred in the vertical x'-z plane, which indicates that the bubble moved in $\boldsymbol{t}$ and $\boldsymbol{n}$ directions. The bubble's minor axis was almost aligned with the motion direction ($\boldsymbol{t}$). Thus, it is possible to obtain the components of $\boldsymbol{u}$ and $\boldsymbol{\Psi}$ in the $\boldsymbol{t}$, $\boldsymbol{n}$, and $\boldsymbol{b}$ directions as

$$u_t = \frac{ds}{dt}, \quad u_n = 0, \quad u_b = 0, \tag{9}$$

$$\Psi_t = 0, \quad \Psi_n = 0, \quad \Psi_b = \frac{d\theta}{dt}, \tag{10}$$

where s is the displacement of the bubble and θ is the pitch angle of the path. Then, the motion equations in the $\boldsymbol{t}$ and $\boldsymbol{n}$ directions can be written as

$$(\rho_b + C_m \rho_w)\frac{\pi}{6} d^3 \frac{d^2 s}{dt^2} = F_t + F_{Bt} \tag{11}$$

and

$$(\rho_b + C_m\rho_w)\frac{\pi}{6}d^3\frac{d\theta}{dt}\frac{ds}{dt} = F_n + F_{Bn}. \tag{12}$$

Here, C_m is the added mass coefficient, which has been found to depend only on the geometry and instantaneous relative acceleration of the body [23,65–67], and it can be obtained analytically from the potential flow solution, as derived by Lamb [63],

$$C_m = \frac{(\chi^2-1)^{1/2} - \cos^{-1}\chi^{-1}}{\cos^{-1}\chi^{-1} - \chi^{-2}(\chi^2-1)^{1/2}}. \tag{13}$$

F_{Bt} and F_{Bn} are the components of the buoyancy F_B in the $\boldsymbol{t}$ and $\boldsymbol{n}$ directions,

$$F_{Bt} = F_B\cos\theta, \quad F_{Bn} = F_B\sin\theta, \tag{14}$$

and F_t and F_n are the components of the hydrodynamic force F_H in the $\boldsymbol{t}$ and $\boldsymbol{n}$ directions, which can be calculated by combining Eqs. (11)–(14).

The force components in the $\boldsymbol{b}$ direction, orthogonal to the zigzagging motion plane t-n, are negligible in comparison, making the lift force induced by the asymmetric wakes $F_L = F_n$. The wake-induced drag $F_{D\omega}$ due to the asymmetry can be obtained by deducting the drag F_{D0} if the bubble's wake were axisymmetric from F_t [23]. We evaluate F_{D0} using the drag coefficient C_{D0} assuming an axisymmetric wake [20] as shown in Fig. 4(b), i.e., $F_{D0} = -C_{D0}\pi d^2\rho_w u^2/8$. Thus,

$$F_{D\omega} = F_t + C_{D0}\frac{\pi}{8}d^2\rho_w u^2, \tag{15}$$

and the wake-induced force due to the asymmetric effect can be expressed as

$$F_\omega = \left(F_L^2 + F_{D\omega}^2\right)^{1/2}. \tag{16}$$

The angle between the "vortex plane" and the bubble motion direction is estimated as follows [64]:

$$\psi = \tan^{-1}\frac{F_{D\omega}}{F_L}. \tag{17}$$

2. Forces acting on an oil-coated bubble

By measuring the displacement and velocity of the rising compound bubbles, the evolution of the forces acting on the compound bubble can be calculated based on Eqs. (11)–(17). Figure 8 shows the time evolution of the magnitudes of the calculated forces, the bubbles' lateral displacement x' and velocity $u_{x'}$, and the pitch angle of the path θ at the zigzag stage. The velocity oscillation frequency was twice the path oscillation frequency f. F_t also oscillated at frequency $2f$, whereas F_L had frequency f; note that the sign of F_L changes with $\boldsymbol{n}$ when the bubble goes through the inflection point of the path. In addition, F_{D0} oscillated simultaneously with the velocity, whereas F_L oscillated synchronously with $F_{D\omega}$, confirming the same inherent physics as wake-induced forces, as shown in Fig. 3(j). The two counter-rotating asymmetric vortices induced low-pressure regions which, compared to the axisymmetric scenario, increased the pressure difference between the front and back regions of the bubble. It generated an additional wake-induced force F_ω perpendicular to the vortex plane [23,64]. The lag between the F_L oscillation (or $F_{D\omega}$) and the path (or velocity) oscillation is due to the counter-rotating vortex pair sign change and shedding between the inflection point and the crest of the path [18].

The magnitudes of F_t with F_{Bt} and F_L with F_{Bn} are very close. The magnitudes of the left terms in Eqs. (11) and (12) are less than $0.1F_B$, which indicates that the inertia term $(m\mathsf{I} + \mathsf{A})d\boldsymbol{u}/dt$ in Eq. (8) is much smaller than the other forces, resulting in a slight variation of the bubble velocity. The magnitude of F_{Bt} and F_{Bn} decreased continuously with ϕ_o due to the increasing ρ_b, which corresponds to the decreasing F_t and F_n.

For compound bubbles rising with a steady path oscillation, $F_{D\omega}$, F_{D0}, and F_L are comparable, indicating the significance of the forces induced by the asymmetric vortex in the compound bubble

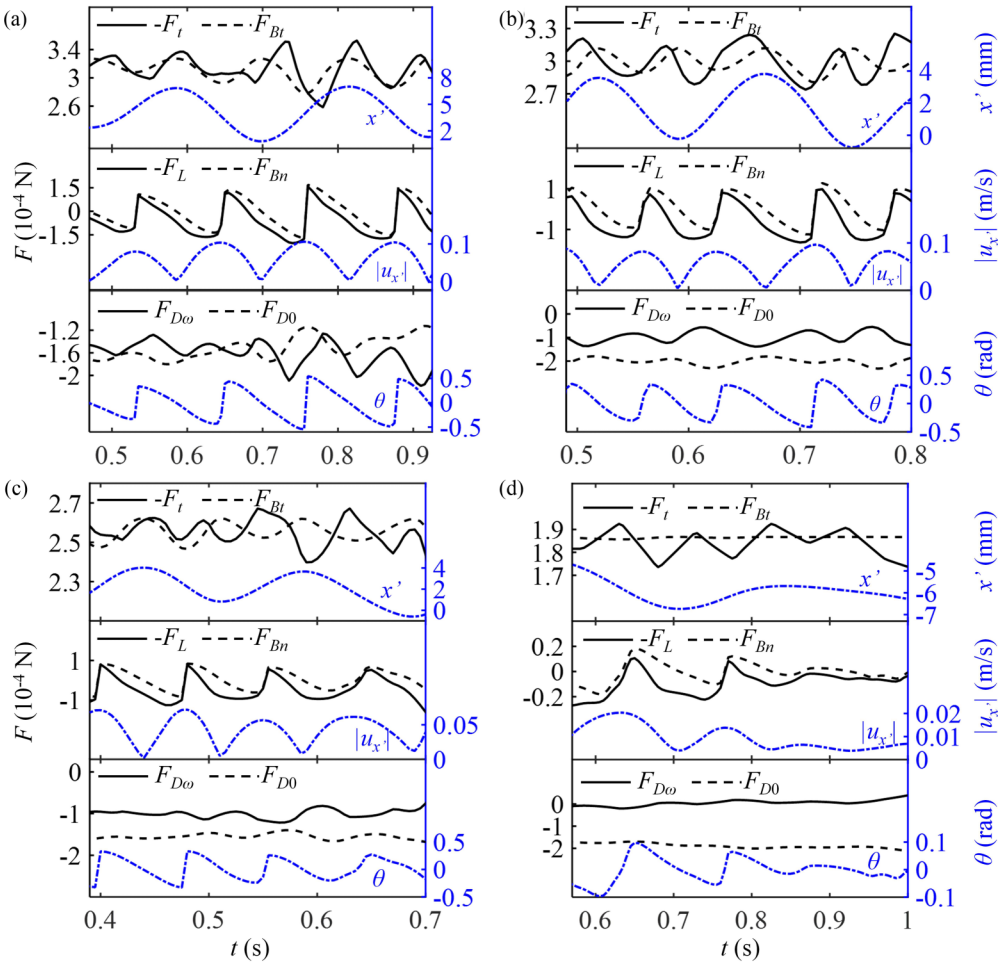

FIG. 8. Time evolution of the acting forces, transverse displacement x' (blue lines in the top subpanels), transverse velocity $u_{x'}$ (blue lines in the middle subpanels), and the pitch angle of the path θ (blue lines in the bottom subpanels) at the zigzag stage for (a) the gas bubble, 10 cSt silicone oil-coated bubbles with oil fractions of (b) 0.08, (c) 0.22, and (d) 0.61. The black-solid and black-dashed lines represent $-F_t$ and F_{Bt} (top subpanels), $-F_L$ and F_{Bn} (middle subpanels), and $F_{D\omega}$ and F_{D0} (bottom subpanels).

dynamics. For the comparatively high ϕ_o bubbles with damped path oscillations, the wake-induced forces $F_{D\omega}$ and F_L were much smaller than F_B at the initial zigzag stage and were quickly damped to near 0, which is consistent with the damped path oscillation. Such a phenomenon indicates that the asymmetry of the vortex suddenly vanishes when ϕ_o is larger than a critical value, causing the oil-coated bubble to return to the rectilinear rising mode.

The time-averaged wake-induced forces $\langle F_{D\omega}\rangle$, $\langle F_L\rangle$, and $\langle F_\omega\rangle$, $(\rho_b + C_m\rho_w)/\rho_w$, and the maximum pitch angle θ_m through the second and the second-to-last peaks in the zigzag stages are shown in Fig. 9, where $\langle\psi\rangle$ is the mean ψ calculated from $\langle F_{D\omega}\rangle$ and $\langle F_L\rangle$. We first note that the effective mass of the bubble during the rising $(\rho_b + C_m\rho_w)\pi d^3/6$ did not change significantly with ϕ_o; thus, the variation of the bubble zigzagging motion was mainly attributed to the external forces. $\langle F_L\rangle$ remained unchanged when the bubble changed from clean to lightly coated, which is consistent with the findings of Tagawa *et al.* [20], whereas $\langle F_{D\omega}\rangle$ and $\langle F_\omega\rangle$ decreased, corresponding to a decreasing $\langle\psi\rangle$. The unchanged $\langle F_L\rangle$ may result from the competition between a more immobile surface and the

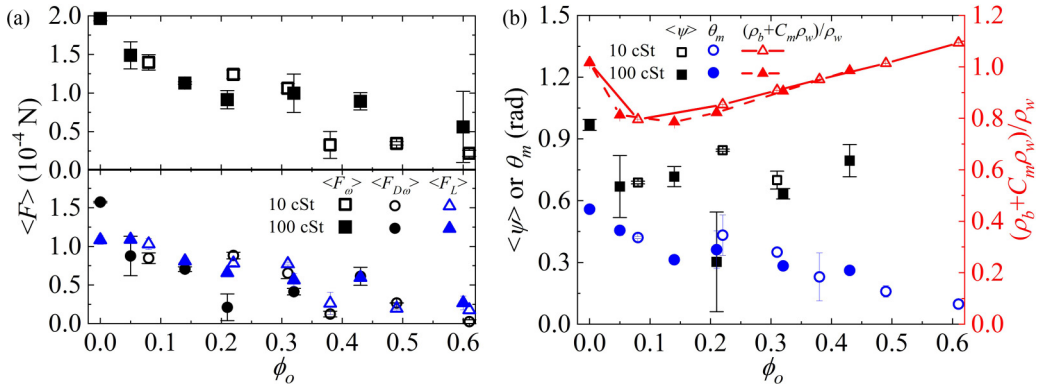

FIG. 9. (a) Time-averaged wake-induced forces $\langle F_{D\omega}\rangle$, $\langle F_L\rangle$, and $\langle F_\omega\rangle$ as a function of the oil fraction ϕ_o; (b) the maximum pitch angle θ_m, the average angle between the "vortex plane" and bubble motion direction $\langle\psi\rangle$, and $(\rho_b + C_m\rho_w)/\rho_w$ as a function of the oil fraction ϕ_o at the zigzag stage.

more spherical bubble shape, generating similar vorticity with smaller $\langle\psi\rangle$ behind the lightly coated bubble compared to that of a clean gas bubble. $\langle F_{D\omega}\rangle$ and $\langle F_L\rangle$ decreased with ϕ_o, resulting in smaller $\langle F_\omega\rangle$ and constant $\langle\psi\rangle$ for oil-coated bubbles with a steady path oscillation, confirming that bubbles with smaller deformation generate weaker vorticity. The evolution of $\langle F_L\rangle$ with ϕ_o also supports our discussion on the bubble oscillation amplitude in Sec. III B 4. We also note an average $\langle\psi\rangle \approx 38^\circ$ for the steady oscillation oil-coated bubbles, while Veldhuis *et al.* [64] obtained a similar ψ within 25°–38° for the zigzagging and spiral rising of buoyant solid spheres. The wake-induced forces vanished for a comparatively high ϕ_o bubble with a damped path oscillation; thus, their $\langle\psi\rangle$ are not shown in Fig. 9(b). Furthermore, the maximum pitch angle θ_m decreased with ϕ_o, corresponding to a more rectilinear path of the high ϕ_o bubbles.

In addition to the changes of the velocity boundary condition and the effective density of the bubble, other factors induced by the oil coating may also affect the path/wake instability of the rising oil-coated bubble. In Eq. (8), we assume the shape centroid of the compound bubble as its mass centroid (no mass eccentricity), resulting in a minor wake-induced force on the oil-coated bubbles with weaker path oscillations. However, considering the large oil-gas density ratios ($\approx 10^3$), the mass center of the compound bubble may deviate from the shape centroid, yielding mass eccentricity. The ratio of the compound bubble mass (the portion causing the mass eccentricity) in the effective mass in Eqs. (11) and (12), $\rho_b/(\rho_b + C_m\rho_w)$, increased with ϕ_o. The $\rho_b/(\rho_b + C_m\rho_w)$ is nearly 0 for lightly coated bubbles, and 0.37 for the 10 cSt oil-coated bubble with $\phi_o = \phi_{oc} = 0.38$ and 0.52 for the 100 cSt counterpart with $\phi_o = \phi_{oc} = 0.6$. Therefore, the effect of bubble mass eccentricity may play a non-negligible role in the rising dynamics of high ϕ_o bubbles. In fact, Tanaka *et al.* [68] found that an eccentric mass sphere has a weaker lateral migration and rotation compared with a uniform sphere, aligning with our observations as well. A more precise estimation of the wake-induced force can be achieved by taking the mass eccentricity into consideration. Also, increasing ϕ_o enlarges the rotational inertia of the oil-coated bubble. Mathai *et al.* [69] pointed out that buoyant spheres with a high rotational inertia rise with a small path oscillation amplitude and a nearly vertical wake pattern, and they suggested that the rotational inertia is an additional factor that triggers the path instability; it may deserve further investigation in the context of a rising oil-coated bubble and its wake.

D. Damped oscillation

One of the distinct features of rising oil-coated bubbles is the significant damped oscillation when $\phi_o \geqslant \phi_{oc}$, with a transverse amplitude decaying with time. The damped bubble's oscillation was interpreted in terms of the harmonic component and the background trend (triggered by

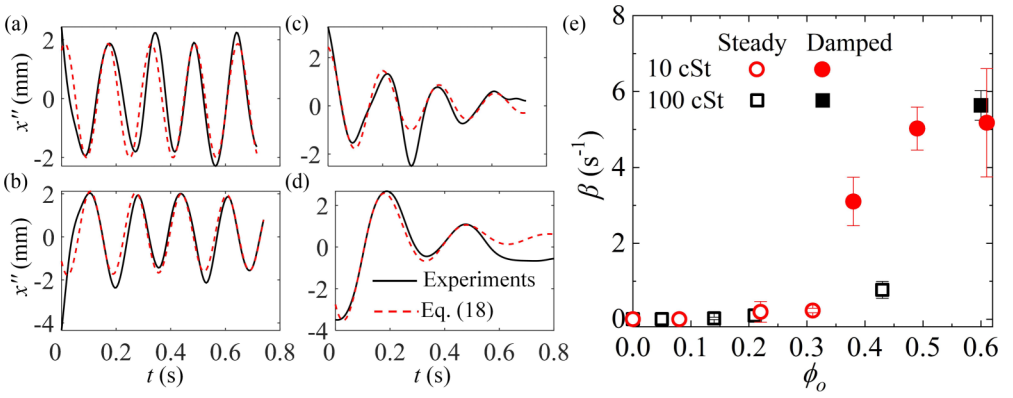

FIG. 10. Experimentally obtained (solid lines) and model predicted [Eq. (18), dashed lines] time evolution of the transverse displacement x'' of the 10 cSt oil-coated bubbles with (a) oil fraction $\phi_o = 0.08$, $A_0 = 1.94$ mm, $\beta = 0$, $\omega = 6.32$ s^{-1}, and $\varphi = 1.07$; (b) $\phi_o = 0.31$, $A_0 = 1.98$ mm, $\beta = 0.19$ s^{-1}, $\omega = 6.00$ s^{-1}, and $\varphi = 3.87$; (c) $\phi_o = 0.38$, $A_0 = 2.39$ mm, $\beta = 2.65$ s^{-1}, $\omega = 4.86$ s^{-1}, and $\varphi = 1.63$; and (d) $\phi_o = 0.61$, $A_0 = 4.57$ mm, $\beta = 4.17$ s^{-1}, $\omega = 3.32$ s^{-1}, and $\varphi = 3.92$. (e) Dependence of the damping coefficient β on ϕ_o for 10 (circle) and 100 cSt (square) oil-coated bubbles. The open and solid points represent the steady oscillation and damped oscillation, respectively.

releasing uncertainty). Hence, it was convenient to detrend the time series of the bubble's transverse displacement x' by spline interpolation of the local maxima and minima to accurately calculate the equilibrium position [70,71]. Then, the function for damped harmonic motion was used to quantify the damping rate:

$$x'' = A_0 e^{-\beta t} \sin(2\pi\omega t + \varphi), \tag{18}$$

where x'' is the bubble's transverse displacement after detrend, A_0 is the initial oscillation amplitude, β is the damping coefficient, ω is the oscillation frequency, and φ is the initial phase. Figures 10(a)–10(d) show the evolution of x'' with t for 10 cSt oil-coated bubbles with different ϕ_o. Equation (18) describes the experimental results well. The oscillation of x'' is basically unchanged for oil-coated bubbles with $\phi_o < \phi_{oc}$, while it damps significantly for oil-coated bubbles with $\phi_o \geqslant \phi_{oc}$, and the bubble's trajectory quickly returns to rectilinear after several path oscillations. The dependence of the damping coefficient β on ϕ_o for 10 and 100 cSt oil-coated bubbles is shown in Fig. 10(e). $\beta \approx 0$ when $\phi_o < \phi_{oc}$, and suddenly increases across the critical oil fraction ϕ_{oc}, indicating the occurrence of damped oscillation. Although in the previous discussion the shape deformation, drag coefficient, and path oscillation frequency are similar for 10 and 100 cSt oil-coated bubbles, the ϕ_{oc} of the damped oscillation is different.

The occurrence of the damped oscillation may be attributed to the oil tail sloshing during zigzagging, which cannot be fully described by the model in Sec. III C 2. As shown in Fig. 5, the oil coating is always sloshed to the outer side of the trajectory at the zigzag stage. The oil sloshing occurred whenever the motion direction and acceleration of the compound bubble changed, altering the mass center and the rotational inertia of the compound bubble dynamically. Mathai *et al.* [72] reported that the dynamics and wake of a freely rising cylinder are governed by its density ratio (ρ_b/ρ_w) and rotational inertia. They stated that the two-pair (2P) vortex mode transition to the two-single (2S) vortex mode occurs when the density ratio increases to 0.2–1, depending on the rotational inertia. The corresponding cylinder path varies from a zigzagging mode to a nearly rectilinear mode. The sudden appearance of path oscillations has also been found experimentally for a freely rising sphere with a critical mass ratio of about 0.61 [73,74]. Here, the density ratio of the compound bubble, $\rho_b/\rho_w \approx \phi_o$, varied between 0.05 and 0.61. From the PIV measurements, we observed a transition of the wake from 2P- to 2S-like modes along the damped oscillation

TABLE II. Formation system parameters of the bubbles in Figs. 3 and 4 and Figs. 6– 9. OD represents the outer diameter of the outer needle, whereas the inner diameter of the inner needles is fixed (0.4 mm). The gas bubble (Case 1) was generated using a stainless blunt needle of with an inner diameter of 1.4 mm.

Case	d (mm)	ϕ_o	ρ_b (kg m^{-3})	Oil viscosity (cSt)	OD (mm)	V_o^i (μL)
1	4.00	0	1.2	N/A	N/A	N/A
2	4.00	0.08	75.5	10	4.2	10
3	4.00	0.22	205.6	10	4.2	20
4	4.08	0.31	289.1	10	4.2	30
5	4.02	0.38	354.2	10	2.8	30
6	4.07	0.49	456.3	10	2.1	20
7	4.39	0.61	567.8	10	2.1	30
8	4.07	0.05	49.2	100	3.4	6
9	4.04	0.14	135.5	100	3.4	13
10	4.00	0.21	202.6	100	3.4	26
11	4.04	0.32	308.0	100	3.4	30
12	4.07	0.43	413.5	100	2.8	33
13	4.45	0.60	576.5	100	2.1	30

trajectory for bubbles with $\phi_o \geqslant \phi_{oc}$; see Fig. 6(d). By modulating the bubble's mass center and rotational inertia dynamically, the oil sloshing during zigzagging may trigger the occurrence of the transition of wake dynamics for the rising compound bubble with a high ϕ_o. More viscous oil sloshed less in our experiments, making ϕ_{oc} for 10 cSt silicone oil-coated bubbles smaller than 100 cSt silicone oil-coated bubbles. Uncovering the specific physics in the damped oscillation requires further modeling to include all the above factors.

IV. CONCLUSION

In this work, we experimentally investigate the rising dynamics of an oil-coated bubble in quiescent liquid. We observe that the oil-coated bubbles experience first steady oscillations followed by damped zigzagging paths with increasing oil volume fraction ϕ_o. The oil coating alters the bubble rising dynamics mainly by changes in the bubble surface boundary condition and effective density. Compared with a gas bubble, oil coating not only effectively exerts a nearly immobile surface on the bubble enhancing flow separation, but also significantly decreases the shape deformation weakening the vorticity generation. Therefore, a lightly coated bubble has similar drag coefficient and wake-induced lift force but a larger frequency and smaller amplitude path oscillation. An increase of ϕ_o of the oil-coated bubbles results in a decrease of the density difference between the oil-coated bubble and the bulk liquid; then, it further inhibits the shape deformation as well as the vorticity generation. Comparatively large ϕ_o bubbles have reduced drag coefficient and wake-induced lift force, thus they rise with a smaller frequency and amplitude of path oscillation than small ϕ_o bubbles.

Our findings contribute to the fundamental understanding of the rising dynamics of compound bubbles, including the path instability and wake-induced forces, and they may provide guidance for simulations and practical applications of bubbly flows with compound interfaces. Physical mechanisms inducing path oscillation damping for large ϕ_o should be further explored; in particular, mass eccentricity, rotational motion, oil sloshing, and wake dynamics are contributing factors that remain to be considered in future research. In addition, we note that the compound bubbles studied here are fully engulfed considering the complete wetting state of the silicone oil at the water/air surface. However, with different wetting states of the oil at the gas bubble surface, a "Janus bubble" can also be produced when the gas bubble surface is partially covered by the oil [10]. Such a change

may impose a different velocity boundary condition along the bubble surface, and thus how the wetting state affects the rising dynamics requires further work.

ACKNOWLEDGMENTS

B.J. would like to thank Yujia Zhou for the helpful discussion. This work is partially supported by American Chemical Society Petroleum Research Fund Grant No. 61574-DNI9 (to J.F.).

APPENDIX: TABULATED: BUBBLE FORMATION PROPERTIES

In this Appendix, we provide the formation system parameters of the bubbles presented in Figs. 3 and 4 and Figs. 7–9 in a tabulated form. Table II lists the bubble diameter d, oil fraction ϕ_o, oil viscosity, the bubble density ρ_b calculated by Eq. (3), the coaxial orifices size, and the initial oil volume V_o^i. The inner diameter of the inner needles is fixed as 0.41 mm and the outer diameters of the outer needles (OD) are listed in Table II. The gas bubble (Case 1) was generated using a stainless blunt needle with an inner diameter of 1.4 mm.

[1] R. E. Johnson and S. S. Sadhal, Fluid mechanics of compound multiphase drops and bubbles, Annu. Rev. Fluid Mech. **17**, 289 (1985).
[2] S. S. Sadhal, P. S. Ayyaswamy, and J. N. Chung, *Transport Phenomena with Drops and Bubbles* (Springer Science & Business Media, New York, 2012).
[3] C. Johansen, A. C. Todd, and I. R. MacDonald, Time series video analysis of bubble release processes at natural hydrocarbon seeps in the northern gulf of mexico, Marine Petroleum Geology **82**, 21 (2017).
[4] F. Zhou, L. Wang, Z. Xu, Q. Liu, M. Deng, and R. Chi, Application of reactive oily bubbles to bastnaesite flotation, Miner. Eng. **64**, 139 (2014).
[5] L. Su, Z. Xu, and J. Masliyah, Role of oily bubbles in enhancing bitumen flotation, Miner. Eng. **19**, 641 (2006).
[6] T. S. Emery, P. A. Raghupathi, and S. G. Kandlikar, Bubble growth inside an evaporating liquid droplet introduced in an immiscible superheated liquid, Int. J. Heat Mass Transf. **127**, 313 (2018).
[7] A. A. Kulkarni and V. V. Ranade, Direct contact heat transfer via injecting volatile liquid in a hot liquid pool: Generation and motion of bubbles, Chem. Eng. Sci. **100**, 421 (2013).
[8] G. R. Moore, Vaporization of superheated drops in liquids, AIChE J. **5**, 458 (1959).
[9] C. W. Visser, D. N. Amato, J. Mueller, and J. A. Lewis, Architected polymer foams via direct bubble writing, Adv. Mater. **31**, 1904668 (2019).
[10] Y. H. Mori, Configurations of gas-liquid two-phase bubbles in immiscible liquid media, Int. J. Multiphase Flow **4**, 383 (1978).
[11] D. C. Blanchard and L. Syzdek, Mechanism for the water-to-air transfer and concentration of bacteria, Science **170**, 626 (1970).
[12] D. C. Blanchard, The ejection of drops from the sea and their enrichment with bacteria and other materials: A review, Estuaries **12**, 127 (1989).
[13] P. L. L. Walls and J. C. Bird, Enriching particles on a bubble through drainage: Measuring and modeling the concentration of microbial particles in a bubble film at rupture, Elementa-Sci. Anthrop. **5**, 34 (2017).
[14] S. H. Behrens, Oil-coated bubbles in particle suspensions, capillary foams, and related opportunities in colloidal multiphase systems, Curr. Opin. Colloid Interface Sci. **50**, 101384 (2020).
[15] B. Ji, Z. Yang, and J. Feng, Compound jetting from bubble bursting at an air-oil-water interface, Nat. Commun. **12**, 6305 (2021).
[16] G. Mougin and J. Magnaudet, Path Instability of a Rising Bubble, Phys. Rev. Lett. **88**, 014502 (2001).
[17] P. C. Duineveld, The rise velocity and shape of bubbles in pure water at high reynolds number, J. Fluid Mech. **292**, 325 (1995).

[18] J. C. Cano-Lozano, C. Martinez-Bazan, J. Magnaudet, and J. Tchoufag, Paths and wakes of deformable nearly spheroidal rising bubbles close to the transition to path instability, Phys. Rev. Fluids **1**, 053604 (2016).
[19] C. Veldhuis, A. Biesheuvel, and L. Van Wijngaarden, Shape oscillations on bubbles rising in clean and in tap water, Phys. Fluids **20**, 040705 (2008).
[20] Y. Tagawa, S. Takagi, and Y. Matsumoto, Surfactant effect on path instability of a rising bubble, J. Fluid Mech. **738**, 124 (2014).
[21] S. Takagi and Y. Matsumoto, Surfactant effects on bubble motion and bubbly flows, Annu. Rev. Fluid Mech. **43**, 615 (2011).
[22] W. L. Shew, S. Poncet, and J.-F. Pinton, Force measurements on rising bubbles, J. Fluid Mech. **569**, 51 (2006).
[23] G. Mougin and J. Magnaudet, Wake-induced forces and torques on a zigzagging/spiralling bubble, J. Fluid Mech. **567**, 185 (2006).
[24] E. Loth, Quasi-steady shape and drag of deformable bubbles and drops, Int. J. Multiphase Flow **34**, 523 (2008).
[25] Y. Zhou, C. Zhao, and H. Bo, Analyses and modified models for bubble shape and drag coefficient covering a wide range of working conditions, Int. J. Multiphase Flow **127**, 103265 (2020).
[26] W. L. Shew and J.-F. Pinton, Dynamical Model of Bubble Path Instability, Phys. Rev. Lett. **97**, 144508 (2006).
[27] Y. Zhou, C. Zhao, B. Ji, and H. Bo, Numerical simulation of bubbly flow using partially averaged navier-stokes simulation and a path oscillation model in the euler-lagrange approach, Ind. Eng. Chem. Res. **60**, 4120 (2021).
[28] S. R. Adoua, D. Legendre, and J. Magnaudet, Reversal of the lift force on an oblate bubble in a weakly viscous linear shear flow, J. Fluid Mech. **628**, 23 (2009).
[29] V. Mathai, S. G. Huisman, C. Sun, D. Lohse, and M. Bourgoin, Dispersion of Air Bubbles in Isotropic Turbulence, Phys. Rev. Lett. **121**, 054501 (2018).
[30] V. Mathai, D. Lohse, and C. Sun, Bubbly and buoyant particle–laden turbulent flows, Annu. Rev. Condens. Matter Phys. **11**, 529 (2020).
[31] S. S. Sadhal and R. E. Johnson, Stokes flow past bubbles and drops partially coated with thin films. part 1. stagnant cap of surfactant film–exact solution, J. Fluid Mech. **126**, 237 (1983).
[32] R. E. Johnson and S. S. Sadhal, Stokes flow past bubbles and drops partially coated with thin films. part 2. thin films with internal circulation–a perturbation solution, J. Fluid Mech. **132**, 295 (1983).
[33] S. S. Sadhal and H. N. Oguz, Stokes flow past compound multiphase drops: The case of completely engulfed drops/bubbles, J. Fluid Mech. **160**, 511 (1985).
[34] S. Kawano and H. Hashimoto, Drag coefficient of a spherical encapsulated liquid drop, JSME Int. J., Ser. 2 **35**, 151 (1992).
[35] S. Kawano, H. Hashimoto, and T. Suyama, Buoyancy-driven accelerated motion of an encapsulated liquid drop, JSME Int. J., Ser. B **37**, 30 (1994).
[36] B. A. Abdul-Majeed and H. B. Eliwy, Dynamics of a single condensing two-phase bubble, Iraqi J. Chem. Petrol Eng. **8**, 7 (2007).
[37] H. B. Mahood, A. N. Campbell, R. B. Thorpe, and A. O. Sharif, A new model for the drag coefficient of a swarm of condensing vapour–liquid bubbles in a third immiscible liquid phase, Chem. Eng. Sci. **131**, 76 (2015).
[38] S. Wang, Y. Zhang, J. C. Meredith, S. H. Behrens, M. K. Tripathi, and K. C. Sahu, The dynamics of rising oil-coated bubbles: Experiments and simulations, Soft Matter **14**, 2724 (2018).
[39] J. R. Karp, E. Mancilla, F. S. da Silva, D. Legendre, R. Zenit, and R. E. M. Morales, The dynamics of compound drops at high reynolds numbers: Drag, shape, and trajectory, Int. J. Multiphase Flow **142**, 103699 (2021).
[40] H. Kong, H. C. Akakin, and S. E. Sarma, A generalized laplacian of gaussian filter for blob detection and its applications, IEEE T Cybernetics **43**, 1719 (2013).
[41] J. C. Crocker and D. G. Grier, Methods of digital video microscopy for colloidal studies, J. Coll. Interface Sci. **179**, 298 (1996).

[42] P. Craven and G. Wahba, Smoothing noisy data with spline functions, Numer. Math. **31**, 377 (1978).
[43] J.-T. Kim, S. Shen, S. L. DiMarco, Y. Jin, and L. P. Chamorro, Lagrangian acceleration in Rayleigh-Bénard convection at various aspect ratios, Phys. Rev. Fluids **3**, 113502 (2018).
[44] B. Ji, Z. Yang, and J. Feng, Oil-coated bubble formation from submerged coaxial orifices, Phys. Rev. Fluids **6**, 033602 (2021).
[45] B. Ji, A. Singh, and J. Feng, Oil column pinch-off controls the oil fraction of the oil-coated bubble, Phys. Fluids **33**, 103316 (2021).
[46] S. Aoyama, K. Hayashi, S. Hosokawa, and A. Tomiyama, Shapes of ellipsoidal bubbles in infinite stagnant liquids, Int. J. Multiphase Flow **79**, 23 (2016).
[47] S. Kawano and H. Hashimoto, A numerical study on motion of a sphere coated with a thin liquid film at intermediate reynolds numbers, J. Fluids Eng. **119**, 397 (1997).
[48] R. Clift, J. R. Grace, and M. E. Weber, *Bubbles, Drops, and Particles* (Courier, Mineola, New York, 2005).
[49] M. Ringnér, What is principal component analysis? Nat. Biotechnol. **26**, 303 (2008).
[50] J. C. Cano-Lozano, P. Bohorquez, and C. Martínez-Bazán, Wake instability of a fixed axisymmetric bubble of realistic shape, Int. J. Multiphase Flow **51**, 11 (2013).
[51] M. K. Tripathi, K. C. Sahu, and R. Govindarajan, Dynamics of an initially spherical bubble rising in quiescent liquid, Nat. Commun. **6**, 6268 (2015).
[52] J. B. Will, V. Mathai, S. G. Huisman, D. Lohse, C. Sun, and D. Krug, Kinematics and dynamics of freely rising spheroids at high reynolds numbers, J. Fluid Mech. **912**, A16 (2021).
[53] D. W. Moore, The velocity of rise of distorted gas bubbles in a liquid of small viscosity, J. Fluid Mech. **23**, 749 (1965).
[54] B. Ji, Q. Song, and Q. Yao, Impact of hydrophobic micron ellipsoids on liquid surfaces, J. Colloid Interface Sci. **532**, 711 (2018).
[55] E. Loth, Drag of non-spherical solid particles of regular and irregular shape, Powder Technol. **182**, 342 (2008).
[56] P. Wang, J. J. Cilliers, S. J. Neethling, and P. R. Brito-Parada, Effect of particle size on the rising behavior of particle-laden bubbles, Langmuir **35**, 3680 (2019).
[57] Y. Wang, D. T. Papageorgiou, and C. Maldarelli, Using surfactants to control the formation and size of wakes behind moving bubbles at order-one reynolds numbers, J. Fluid Mech. **453**, 1 (2002).
[58] L. Sirovich, Turbulence and the dynamics of coherent structures. i. coherent structures, Q. Appl. Math. **45**, 561 (1987).
[59] K. Taira, S. L. Brunton, S. T. M. Dawson, C. W. Rowley, T. Colonius, B. J. McKeon, O. T. Schmidt, S. Gordeyev, V. Theofilis, and L. S. Ukeiley, Modal analysis of fluid flows: An overview, AIAA J. **55**, 4013 (2017).
[60] I. Khabbouchi, H. Fellouah, M. Ferchichi, and M. S. Guellouz, Effects of free-stream turbulence and reynolds number on the separated shear layer from a circular cylinder, J. Wind Eng. Indust. Aerodyn. **135**, 46 (2014).
[61] J. Zhou, R. J. Adrian, S. Balachandar, and T. M. Kendall, Mechanisms for generating coherent packets of hairpin vortices in channel flow, J. Fluid Mech. **387**, 353 (1999).
[62] G. K. Batchelor, *An Introduction to Fluid Dynamics* (Cambridge University Press, Cambridge, 1967).
[63] H. Lamb, *Hydrodynamics*, 6th ed. (Dover, New York, 1945).
[64] C. H. J. Veldhuis, A. Biesheuvel, and D. Lohse, Freely rising light solid spheres, Int. J. Multiphase Flow **35**, 312 (2009).
[65] J. C. Wu, Theory for aerodynamic force and moment in viscous flows, AIAA J. **19**, 432 (1981).
[66] L. Quartapelle and M. Napolitano, Force and moment in incompressible flows, AIAA J. **21**, 911 (1983).
[67] M. S. Howe, On the force and moment on a body in an incompressible fluid, with application to rigid bodies and bubbles at high and low reynolds numbers, Q. J. Mech. Appl. Math. **48**, 401 (1995).
[68] M. Tanaka, K. Tajiri, H. Nishida, and M. Yamakawa, Effect of eccentric mass distribution on the motion of spherical particles in shear flows, J. Fluids Eng. **142**, 031105 (2020).
[69] V. Mathai, X. Zhu, C. Sun, and D. Lohse, Flutter to tumble transition of buoyant spheres triggered by rotational inertia changes, Nat. Commun. **9**, 1792 (2018).

[70] J. W. Kantelhardt, E. Koscielny-Bunde, H. H. A. Rego, S. Havlin, and A. Bunde, Detecting long-range correlations with detrended fluctuation analysis, Physica A **295**, 441 (2001).
[71] D. J. Pascoe, C. R. Goddard, G. Nisticò, S. Anfinogentov, and V. M. Nakariakov, Coronal loop seismology using damping of standing kink oscillations by mode coupling, Astron. Astrophys. **589**, A136 (2016).
[72] V. Mathai, X. Zhu, C. Sun, and D. Lohse, Mass and Moment of Inertia Govern the Transition in the Dynamics and Wakes of Freely Rising and Falling Cylinders, Phys. Rev. Lett. **119**, 054501 (2017).
[73] R. N. Govardhan and C. H. K. Williamson, Vortex-induced vibrations of a sphere, J. Fluid Mech. **531**, 11 (1999).
[74] M. Horowitz and C. H. K. Williamson, Critical mass and a new periodic four-ring vortex wake mode for freely rising and falling spheres, Phys. Fluids **20**, 101701 (2008).